# Synergistic Effect of In-Situ Al-7075/Al₃Ti Metal Matrix Composites Prepared via Stir-Assisted Ultrasonic Melt Processing Under Dynamic Nucleation

S. V. Sujith[1] · Hansoo Kim[2,3] · Rahul S. Mulik[4] · Hyeonwoo Park[1] · Joonho Lee[1,2,3]

## Abstract

Owing to the high propensity for particle agglomeration, the fabrication of aluminum matrix composites with uniform distribution using casting routes is extremely difficult. In this study, the in-situ development of the $Al_3Ti$ reinforcing phase by employing stir-assisted ultrasonic treatment was utilized to improve the homogeneity, wettability, and thermodynamic stability of the reinforcing particles in an Al-7075 alloy matrix. The in-situ $Al_3Ti$ particles acted as heterogeneous nucleation sites and facilitated grain refinement to form a non-dendritic globular structure compared with the dendritic cells of the base alloy. The grain size of the $\alpha$-Al dendrites reduced from 160 μm to 65, 50, and 40 μm with the addition of 2, 5, and 7 wt% $Al_3Ti$, respectively. The reduction in the porosity of the composites and the improvement of the particle homogenization were due to cavitation-induced de-agglomeration and the degassing effect. The formation of a robust and clean interface between the $Al_3Ti$ particles and Al alloy via ultrasonic vibration improved the integrity of the composites compared with that of the base alloy. The thermal expansion mismatch between the $Al_3Ti$ particles and Al alloy contributed significantly to the improved mechanical properties of the composites.

## 1 Introduction

In many engineering applications, the demand for discontinuously reinforced metal matrix composites (MMCs) has been increasing because of their high specific strength, high specific modulus, ease of fabrication, high wear resistance, low production cost, and near-isotropic properties [1, 2]. Among the various MMCs used in engineering applications, aluminum matrix composites (AMCs) have been extensively investigated over the past few decades owing to their highly demanding applications in the aerospace, military, and automotive industries [3, 4]. Presently, these sectors are paying attention to weight reduction due to the severe problems associated with the climate change and energy crisis.

Liquid casting methods for the preparation of MMCs involve ex-situ and in-situ routes. In the ex-situ route, the reinforcing ceramic phases are added directly into the melt, while the in-situ method involves the generation of a reinforcing phase in the metal matrix by inducing the chemical reaction of inorganic salts or elemental powders under optimized casting conditions. Recently, the development of the in-situ method has gained attention from various researchers to improve the wettability and thermodynamic stability of conventional ex-situ MMCs. In this process, fine ceramic particles are generated inside the alloy matrix via reaction synthesis [5]. Typical in-situ reinforcements, such as $TiB_2$,

✉ Hansoo Kim
  hansookim@korea.ac.kr

✉ Joonho Lee
  joonholee@korea.ac.kr

1  Department of Materials Science and Engineering, Korea University, Seoul 02841, Republic of Korea

2  Institute for High Technology Materials and Device, Korea University, Seoul 02841, Republic of Korea

3  Center for Research and Education of Metallurgy, Korea University, Seoul 02841, Republic of Korea

4  Department of Mechanical and Industrial Engineering, Indian Institute of Technology Roorkee, Uttrakhand 247667, India

TiC, $Mg_2Si$, $AlB_2$, $Al_2O_3$, $Al_3Ti$, and $ZrB_2$ are synthesized via the salt, direct, and master alloy routes [6].

Various fabrication techniques such as the self-propagating high-temperature synthesis, vacuum pressure infiltration, direct melt laser sintering, stir casting, reactive processing, powder metallurgy, and mechanical alloying, are used for the production of MMCs [7]. Among these processes, the stir casting is most productive and economical for the bulk fabrication of MMCs. Stirring enhances the initial distribution of particles throughout the melt by breaking large clusters of particles to a considerable extent [8]. Together with the stir casting, ultrasonic treatment (UST) has been extensively investigated [9, 10]. Utilization of bubble dynamics, high pressure, high temperature, and acoustic wave propagation leads to a refined microstructure and clean matrix/reinforcement interface. By tuning the ultrasonic parameters, such as the sonication time, frequency, and amplitude, we can achieve good control of the metallurgical and mechanical properties of the composites [11].

There are many reports [14, 15, 17–19] showing the advantage of UST to improve the mechanical and tribological performances of numerous Al alloys due to the refined grain size and increased homogeneity of various reinforcing particles such as $TiB_2$, $ZrB_2$, hexagonal BN and $Al_2Cu$. However, there is a lack of information available on the direct reaction synthesis of in-situ $Al/Al_3Ti$ composites. $Al_3Ti$ exhibits a favorable combination of high Young's modulus (216 GPa), low density (3.4 $g/cm^3$), high melting point (1623 K), and excellent oxidation resistance, and chemical inertness [17]. To the best of our knowledge, there has been no report on the direct reaction synthesis of in-situ

$Al/Al_3Ti$ composites via stir-assisted ultrasonic casting (SUST). Therefore, in this study, we used SUST to develop in-situ $Al-7075/Al_3Ti$ composites by varying the fraction of the reinforcing phase from 2 to 7 wt%. The effect of the $Al_3Ti$ dispersions on the microstructural and mechanical properties of the composites was investigated. Finally, the strengthening effect induced by grain refinement, thermal expansion mismatch, and particle dispersion of the composites was investigated and compared with those of the reference alloy.

## 2 Materials and Methods

### 2.1 Fabrication of In-situ Al-7075/Al$_3$Ti Metal Matrix Composites

A commercial-grade Al-7075 alloy was employed in this study. The composition of the alloy (ANSI H35.1) is presented in Table 1. Figure 1 shows the un-etched microstructure of the Al-7075 base alloy and Ti powder with a purity of 99.8% and an average particle size of 30 μm.
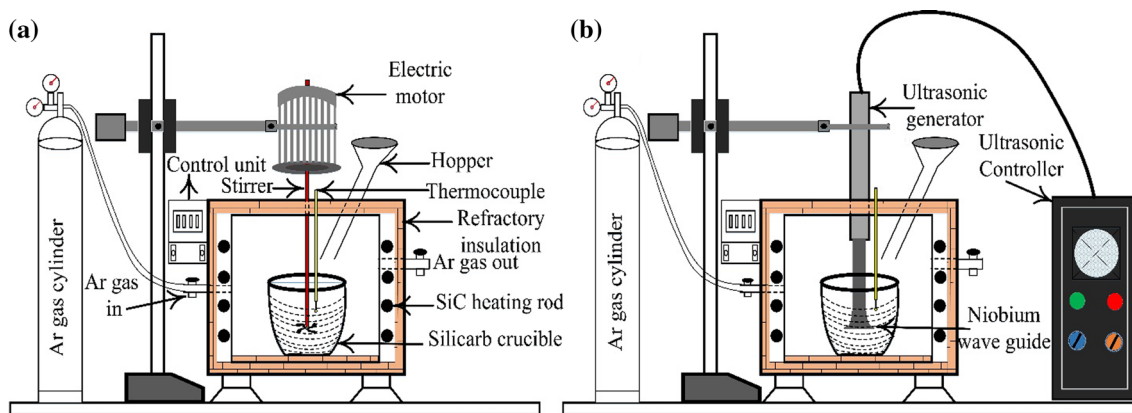
The schematic for the preparation of in-situ Al-7075/ $Al_3Ti$ MMCs via SUST is shown in Fig. 2. Preliminary experiments were conducted on the castings (300 g) to optimize the casting variables to confirm the formation of the $Al_3Ti$ particles without the occurrence of any detrimental reaction inside the matrix alloy. The SUST variables included the stirring time, stirring velocity, holding time, sonication time, sonication frequency, and furnace temperature. Initially, Ti powders were weighed to form 2, 5, and

**Table 1** Chemical composition of the Al-7075 alloy (ANSI H35.1)

| Element | Cr | Cu | Fe | Mn | Mg | Zn | Ti | Si | Al |
|---------|------|------|-----|-----|---------|---------|-----|-----|-----------|
| wt% | 0.18–0.28 | 1.2–2.0 | 0.3 | 0.2 | 2.1–2.9 | 5.1–5.6 | 0.2 | 0.4 | Remaining |
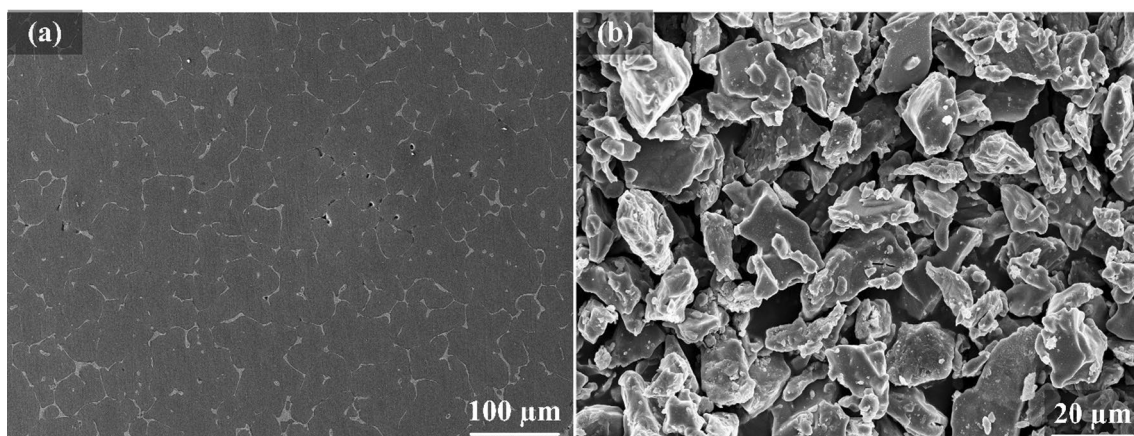


**Fig. 1** Micrographs of the **a** un-etched cast alloy (Al-7075); and **b** Ti powders

**Fig. 2** Schematic for the preparation of the Al-7075/Al₃Ti composites using SUST: **a** conventional mixing setup; and **b** ultrasonication setup

7 wt% $Al_3Ti$ inside the Al-7075 matrix. For example, considering the stoichiometry of $Al_3Ti$, we need to add 0.72 g of Ti powder to form 2 wt% $Al_3Ti$ in 100 g of Al alloy. In real practice, for 1 kg casting, we added (7.2 g + 0.72 g) to induce 2 wt% $Al_3Ti$ formation. The additional 0.72 g was the optimized amount to compensate for the Ti loss caused by the reaction with the flux. The precisely weighed Ti powders were wrapped in an Al foil and preheated to 500 °C in a furnace. A charge of Al-7075 (1 kg) was introduced into a silicon carbide crucible with a diameter of 150 mm and a height of 200 mm. When the melt temperature reached 750 °C, the Ti particles wrapped in the Al foil were added to the melt through the hopper. For the initial homogenization of Ti particles, impeller mixing was performed at 300 rpm for 5 min to ensure the distribution of the particles throughout the melt. To protect the melt from oxidation and atmospheric hydrogen, $CaCl_2$ and $CaF_2$ were added as a covering flux in addition to a continuous supply of argon.

The function of stirring was the fast addition of Ti particles into the melt and the pre-dispersion of the particles for triggering the homogeneous in-situ reaction during the ultrasonication. Once the Ti particles were evenly distributed inside the melt, the melt temperature was raised to 900 °C to initiate the reaction. Before inserting the ultrasonic transducer into the melt, a ($SiO_2$–$TiO_2$)-based coating was deposited onto the horn to prevent the deterioration of both the transducer horn and melt. Then, ultrasonication (20 kHz, 2 kW, 22 µm amplitude, Nb sonotrode) was induced inside the melt for accelerating the even distribution of Ti particles to trigger the in-situ reaction via ultrasonic cavitation. To ensure the complete reaction of Ti particles with Al, the entire melt was isothermally held for 45 min. This was followed by the second ultrasonication step for the final homogenization of the in-situ synthesized $Al_3Ti$ particles throughout the melt. Finally, the melt was poured into a preheated steel mold (500 °C), thereby reducing the extraction of the latent heat and the porosity during the later solidification

process. The time–temperature sequencing involved in the entire casting process is shown in Fig. 3.

## 2.2 Microanalysis

After mechanical polishing, as-cast samples were etched using Keller's reagent (190 mL distilled water, 5 mL $HNO_3$, 3 mL HCl, and 2 mL HF) for 30 s. The microstructural features of the samples were characterized using optical microscopy (Leica DMI 5000 M) and high-resolution field emission scanning electron microscopy (FE-SEM) (Carl Zeiss Ultra Plus) to examine the morphology of the reinforcements and secondary phases. Image J software was used to quantitatively measure the grain size, particle size, and particle frequency of the samples. Total area of 200 µm × 200 µm was observed for the image analysis of particles. The phases of the samples were investigated using X-ray diffraction (XRD) with Cu $K_\alpha$ radiation (Rigaku MiniflexII). The microstructure of the fractured surface was investigated after mechanical testing. The longitudinal surfaces of the fractured samples were extracted from the base matrix and composites to
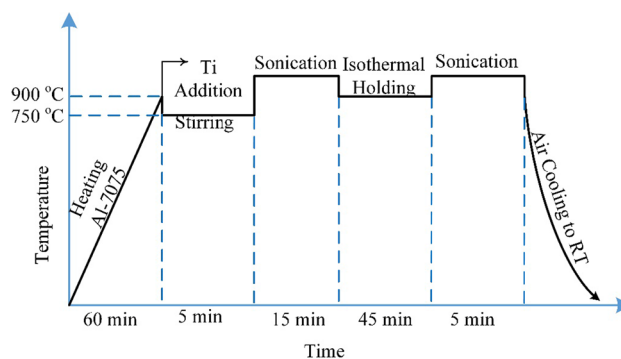


**Fig. 3** Time–temperature sequencing for the preparation of the in-situ Al-7075/Al₃Ti MMCs by SUST

investigate the fracture mechanisms that occurred during the loading process.

## 2.3 Physico-mechanical Property Characterization

Samples were machined from each ingot according to the dimensional specifications for distinctive metallurgical and mechanical tests. To measure the density of the composites, rectangular samples with the dimensions of 30 mm × 30 mm × 10 mm were machined from the base alloy and composites. Then, the selected samples were weighed in air and distilled water of known density using a precision weighing balance with an accuracy of 0.001 g. Tensile tests were conducted at room temperature using ASTM E8 sub-size specimens (gauge length, 25.3 mm; gauge width, 6.4 mm) with a cross-head speed of 1.5 mm/min. The Brinell hardness of the samples was tested using a macro hardness tester HPO 3000 as per ASTM E10-15a. A load of 4.9 kN was applied using a 10-mm ball indenter with a dwell time of 30 s. Ten points were measured with an equal spacing of 11 mm.

## 3 Results

### 3.1 Microstructural Characterization

Figure 4 shows the XRD patterns of the base alloy and composites. The composites showed strong diffraction peaks corresponding to $\alpha$-Al and additional peaks corresponding to the $Al_3Ti$ phase. The $Al_3Ti$ peaks were distinctly clear, and the intensity of the peaks, especially that of the (1 1 2) peak, increased with an increase in the $Al_3Ti$ content. The aluminum oxide phase was not detected because of the efficient protection provided by the argon atmosphere during the casting process. No other intermetallic peaks were observed, confirming that the Ti powder was completely converted into the $Al_3Ti$ reinforcing phase inside the matrix alloy. The composites showed a slight shift in the XRD peaks as compared to the Al-7075 alloy. This can be attributed to the effect of the elastic residual strain, generated during cooling, due to the thermal mismatch between the matrix and reinforcing phase. The $Al_3Ti$ peaks could be well-indexed with JCPDS file No. 00–002-1121. The absence of the peaks corresponding to other intermetallics or other compounds indicates the formation of a thermodynamically stable phase and a contamination-free interface between $Al_3Ti$ and the base matrix.

The optical micrographs of the as-cast alloy and composites are shown in Fig. 5. The as-cast Al-7075 base alloy exhibited a typical dendritic morphology with a high aspect ratio. The dendrite arms were fragmented and redistributed throughout the matrix by the shock waves and melt flow generated by UST, thereby promoting the formation
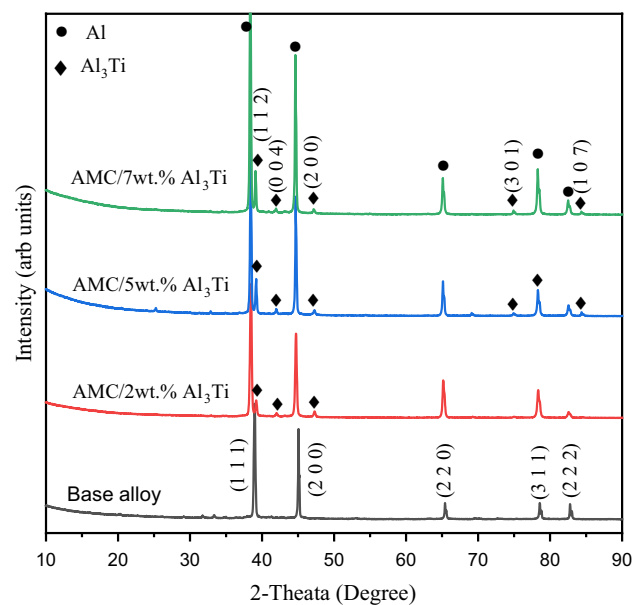


**Fig. 4** XRD patterns of the base alloy and fabricated composites

of numerous nucleation sites in the composites. The average grain size of the base alloy was found to be 160 µm, and the average grain sizes of the composites with 2, 5, and 7 wt% $Al_3Ti$ were 65, 50, and 40 µm, respectively. The dendritic-to-globular morphological transformation and reduced grain size of the primary $\alpha$-Al grains were realized by the combined effect of ultrasonic cavitation and the $Al_3Ti$ particle formation. During the solidification process, these $Al_3Ti$ particles not only acted as the nucleation sites, but also restricted the growth of $\alpha$-Al. Many researchers [18–21] have reported that both $Al_3Ti$ and cavitation-induced nucleation promote grain refinement. The former acts as a heterogeneous nucleation site, and the latter induces high local undercooling, thereby stimulating the nucleation.

The $Al_3Ti$ particle distribution of the composites with different $Al_3Ti$ contents is shown in Fig. 6. The particles had a near-equiaxed blocky shape. In addition, they showed uniform ordering inside the matrix owing to the effect of the UST. Very few particles were observed at the grain boundaries. This is because the particles in the Al melt were forced away from the meniscus owing to the increase in the metallostatic forces. The $Al_3Ti$ particle size distribution in the composites is shown in Fig. 6d. It was found that approximately 50% of the in-situ particles were approximately 5–10 µm in size, and less than 5% of the particles had a size in the range of 25–30 µm. The size distribution of in-situ MMCs is mainly governed by the reaction kinetics between the reactants, stirring time, UST, holding time, and temperature [22–24]. The average particle size was evaluated to be 8 ± 1.5 µm.
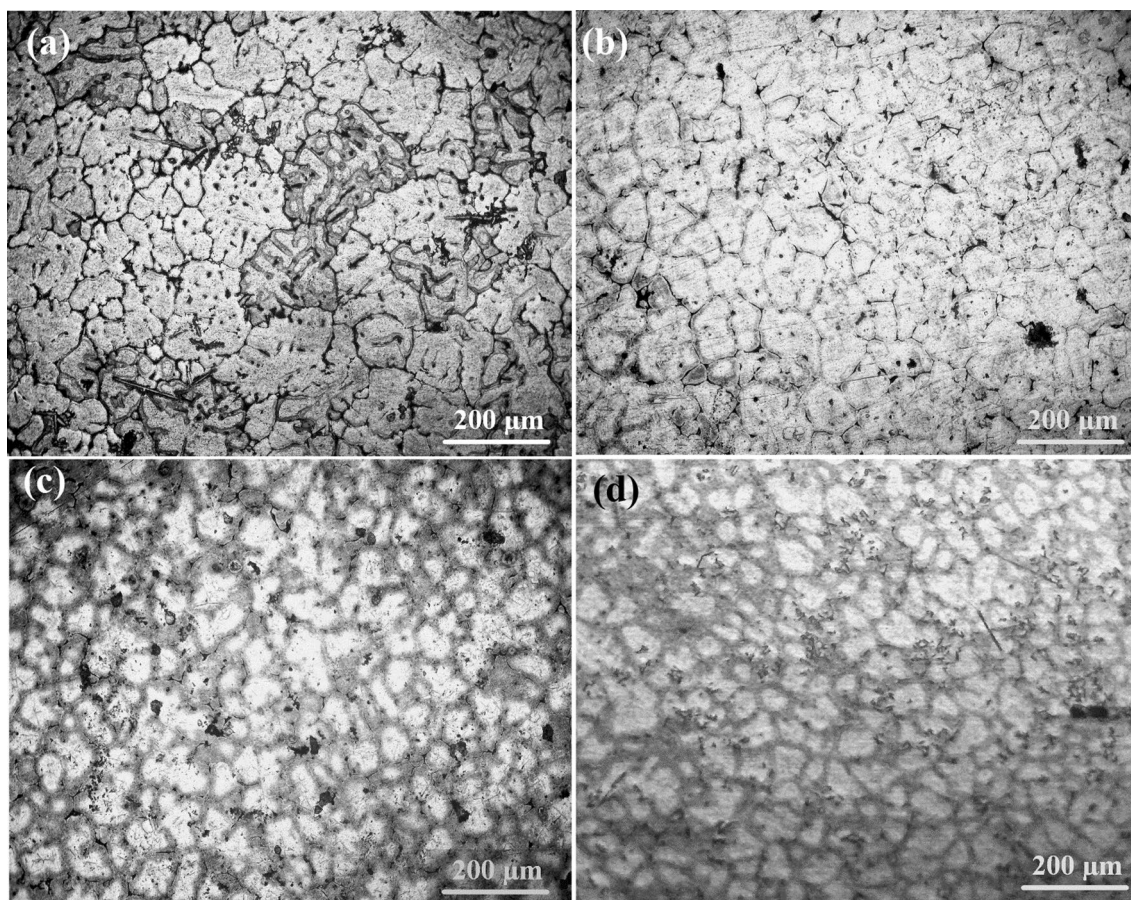
**Fig. 5** Optical micrographs of **a** the as-cast Al-7075 base alloy, **b** Al-7075/2 wt% $Al_3Ti$, **c** Al-7075/5 wt% $Al_3Ti$, and **d** Al-7075/7 wt% $Al_3Ti$

Figure 7a shows the typical as-cast microstructure of the in-situ composites. The evolution of solute-rich phases in Al-Zn-Mg alloys depends on the solidification rate of the molten alloy. According to the EDS analysis shown in Fig. 7d, the white phase regions were rich in Zn, Cu, and Mg. This is believed to be due to the segregation of $MgZn_2$ and $Al_2Mg_3Zn_3$ [25, 26]. The dark gray phase region (Fig. 7b) was rich in Fe and Cu. The liquid region of the Al alloy showed very high Fe solubility, which decreased rapidly in the solid solution of the $\alpha$-Al matrix, limiting up to 0.05 wt% [27]. This was due to the segregation of $Cu_2FeAl_7$ and $FeAl_3$. This result is consistent with those reported previously [28].

To investigate the elemental distributions of the composites, their full area mappings were analyzed, as shown in Fig. 8. The distribution of Ti was detected only in the $Al_3Ti$ particles, which conforms to the reaction of all the Ti powder to form the $Al_3Ti$ particles during the ultrasonic casting, as indicated in Fig. 8e. Mg, Cu, and Zn were detected at the grain boundaries of the $\alpha$-Al matrix.

## 3.2 Physico-mechanical Properties

The experimental densities, theoretical densities, and porosity of the composites with different $Al_3Ti$ contents are shown in Fig. 9. The experimental densities of the cast Al-7075 alloy and in-situ composites were measured using the Archimedes principle [29]. The corresponding theoretical densities were calculated using the rule of mixtures [30].

The density of the composites increased from $2.72 \times 10^3$ to $2.81 \times 10^3$ kg/m$^3$ with an increase in the $Al_3Ti$ content. The porosity of the composites was evaluated from the difference between their theoretical and experimental densities. The porosity of the composites was lower than that of the base alloy. This was mainly due to the degassing efficiency of the UST. The degassing phenomenon occurred in three stages. In the first stage, the dissolved gases in the surrounding crucible were trapped inside the melt, and small bubbles were formed. In the second stage, these bubbles combined to form larger bubbles, which floated on the melt. In the last stage, upon the application of the optimum UST frequency into the melt, these bubbles collapsed to
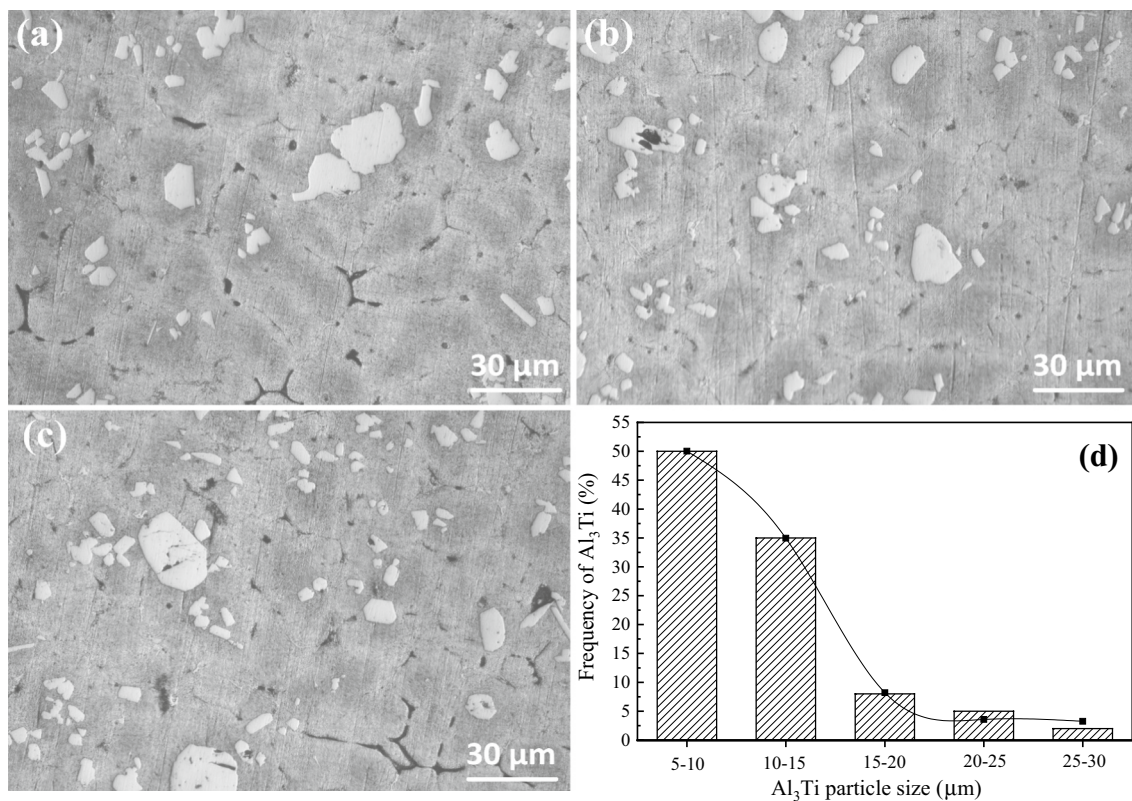
**Fig. 6** Distribution of the Al$_3$Ti particles in **a** Al-7075/2 wt% Al$_3$Ti, **b** Al-7075/5 wt% Al$_3$Ti, **c** Al-7075/7 wt% Al$_3$Ti. **d** the size distribution of Al$_3$Ti particles in the composites

release gas into the environment. This degassing process continued and aided the efficient removal of the entrapped gases in the melt, leading to the formation of composites with less porosity. The porosity decrease with Al$_3$Ti addition may be partly because Al$_3$Ti induces the grain refinement to a great extent by providing with the heterogeneous nucleation sites. In general, fine grains reduce the tendency of micro-porosity formation and hot tearing [31].

The base alloy and the composites with 2, 5, and 7 wt% Al$_3$Ti showed the average hardness values of $117 \pm 4$, $128 \pm 3$, $136 \pm 4$ and $142 \pm 6$ BHN, respectively. The composites with 2, 5, and 7 wt% Al$_3$Ti showed a clear increase of 12.6%, 18.4%, and 22.3%, respectively, in the hardness as compared to the base alloy. The in-situ incorporation of the Al$_3$Ti particles improved the resistance of the composites to plastic deformation due to dispersion strengthening and grain refinement. In addition, the inherent feature of the in-situ fabrication of the Al$_3$Ti particles with clean interfacial bonding between the particles and matrix might also increase the load-bearing capacity of the composites.

The stress vs. strain curves of the base alloy and composites are shown in Fig. 10. The YS and UTS of the composites were 12%–14% and 6%–32% higher than those of the base alloy, respectively. The tensile properties of the composites were governed by the matrix and reinforcement particles.

The major strengthening mechanism of the composites during the tensile loading included grain refinement and dislocation pile up around the Al$_3$Ti particles owing to the thermal stress generated during the solidification process. The homogeneous distribution of particles and impurity-free matrix/reinforcement interface resisted the crack propagation along the interface. The interfacial compatibility aided the transfer of the shear force during the tensile loading. Thus, the load-bearing capacity of the composites was improved. This is because the in-situ Al$_3$Ti did not deform along with the Al-matrix phase and induced stress strain partitioning. A typical strength-ductility tradeoff was observed for all the composites, that is, a substantial decrease in ductility was observed with an increase in the fraction of the Al$_3$Ti phase owing to its brittle nature. The Al$_3$Ti phase has a stable tetragonal D0$_{22}$ crystal structure, which consists of few slip systems, which reduce its ductility. Once the dislocation pile-up around the Al$_3$Ti particles reached its threshold, cracks started propagating and broke the composites under tensile loading. As soon as the cracks nucleated along the interface, instantaneous crack propagation occurred throughout the reinforcement particles owing to their brittle nature.
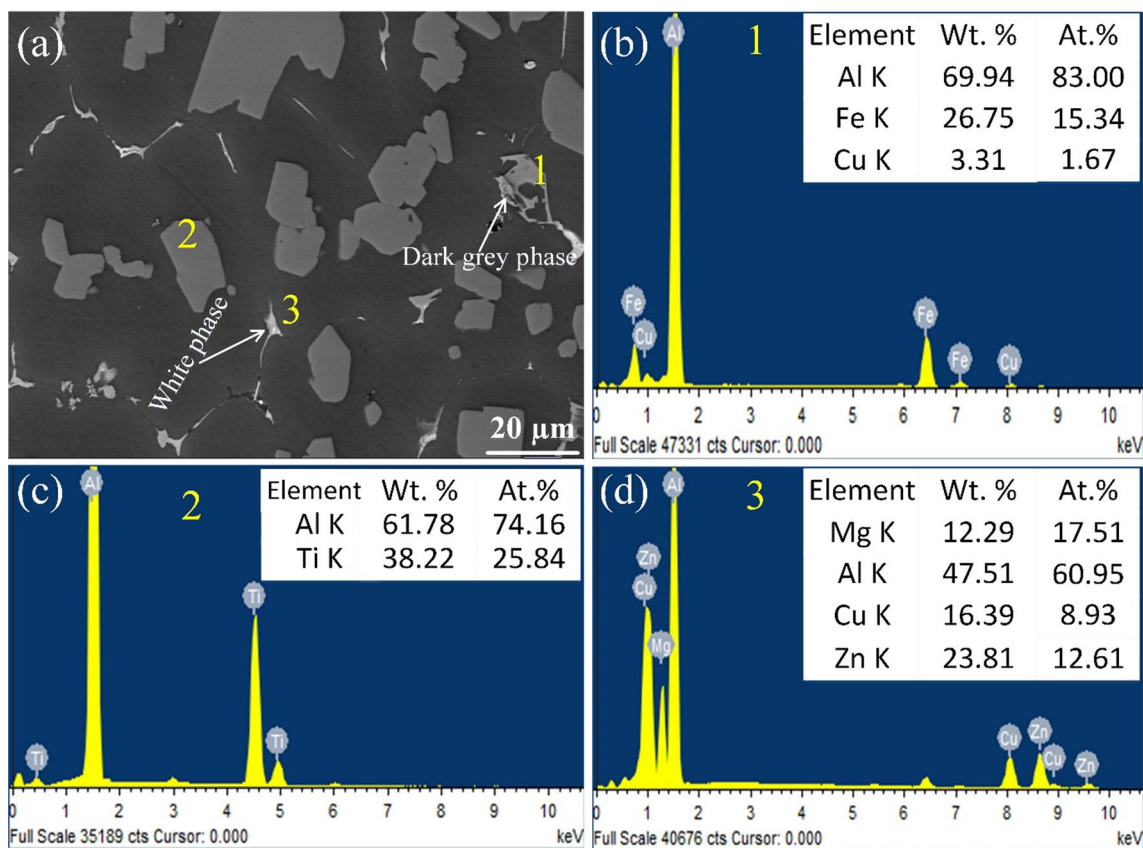
**Fig. 7** Typical SEM image and energy-dispersive X-ray spectroscopy (EDS) profiles of the in-situ Al-7075/Al$_3$Ti cast composites. **a** distribution of the Al$_3$Ti particles and other minor phases (inset: locations of EDS point analysis), **b** dark gray phase, **c** in-situ Al$_3$Ti particles, and **d** white phase

## 3.3 Fractography

The tensile fracture surface of the base alloy is shown in Fig. 11a, which mainly features the inter-dendritic fracture mode. The fine shallow dimples and ductile tear ridges present in the base alloy indicate the ductile fracture mode, as shown in Fig. 11b. Large-sized $\alpha$-Al crystals might have been pulled out during the tensile testing. It can be inferred that large $\alpha$-Al dendrites caused hot tearing during the solidification, which also affected the tensile properties of the base matrix. Interdendritic microporosity was also observed on the fracture surface.

All the composites showed a mixed fracture mode, as shown in Fig. 12. With an increase in the Al$_3$Ti content, the fracture mode of the composites transformed to brittle type with an increase in the tensile strength. Cleavage facets and microvoid coalescence were observed in the composites. Although we have not analyzed the facet plane, it was reported that the cleavage facets in aluminum based composites propagate preferentially along (1 1 1) plane [32]. The fraction of microvoids decreased with an increase in the particle volume fraction. In general, the fracture morphology of the composites was consistent with their tensile behavior.

When the stress reached its elastic limit, the coarse grains started to deform plastically. However, for fine grains, the stress remained under the elastic regime. Thus, the fine-grained microstructures in the composites acted as stress-concentration regions. Once the concentrated stress broke the grain boundaries, the Al$_3$Ti particles arrested further deformation, which increased the stress around the particles until the fracture stress exceeded the interfacial stress. Furthermore, these cracks propagated instantaneously, causing failure under reduced plastic strain as compared to the case of the base alloy matrix. The presence of the Al$_3$Ti particles in the fracture dimples shown in Fig. 12d–f clearly indicates their strong interfacial adhesion with the matrix alloy.
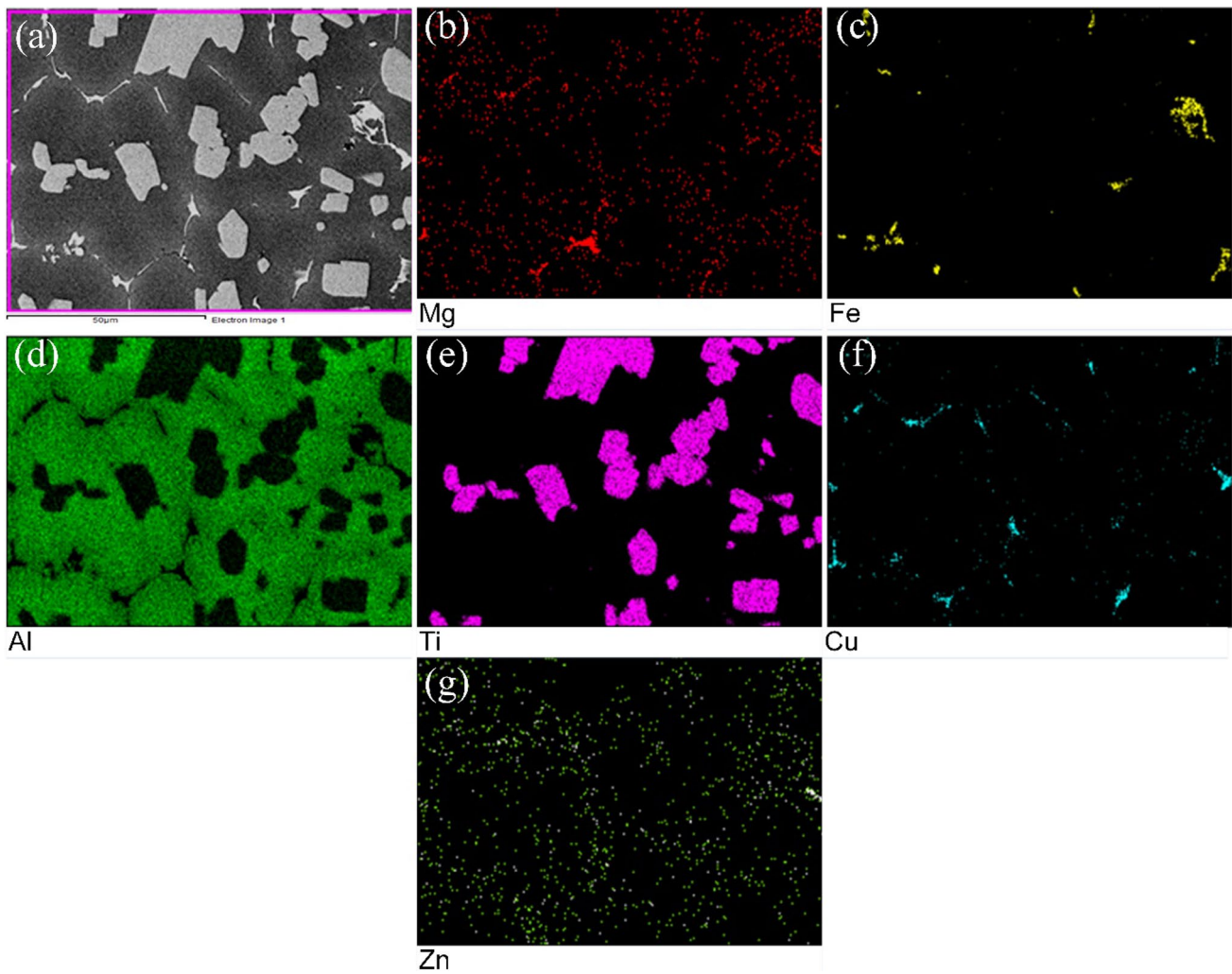
**Fig. 8** Typical FE-SEM/EDS full area mapping of the in-situ Al-7075/Al$_3$Ti cast composites. **a** SEM image with full area selection. **b**–**g** elemental mapping for Mg, Fe, Al, Ti, Cu, and Zn, respectively
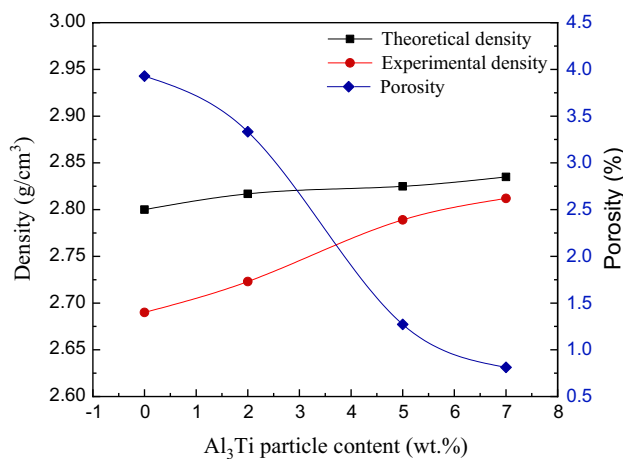


**Fig. 9** Density and porosity of the composites as functions of the Al$_3$Ti particle content

## 4 Discussion

### 4.1 Mechanism of the Formation of In-situ Al$_3$Ti MMCs via SUST

A four-step mechanism is proposed for the formation and distribution of the Al$_3$Ti particles inside the Al melt via SUST: (i) even distribution of Ti particles under impeller stirring (Fig. 13a); (ii) cavitation-induced bubble dynamics. During the UST, alternating high-pressure and low-pressure cycles were successively generated, thereby creating bubbles inside the liquid melt. These bubbles continued to grow over several cycles until they reached their threshold, at which they could not hold more energy. In the subsequent high-pressure cycle, they collapsed vigorously. This violent collapse is known as cavitation, which generates shock waves and local high temperatures inside the melt. The local high temperature accelerated the in-situ reaction
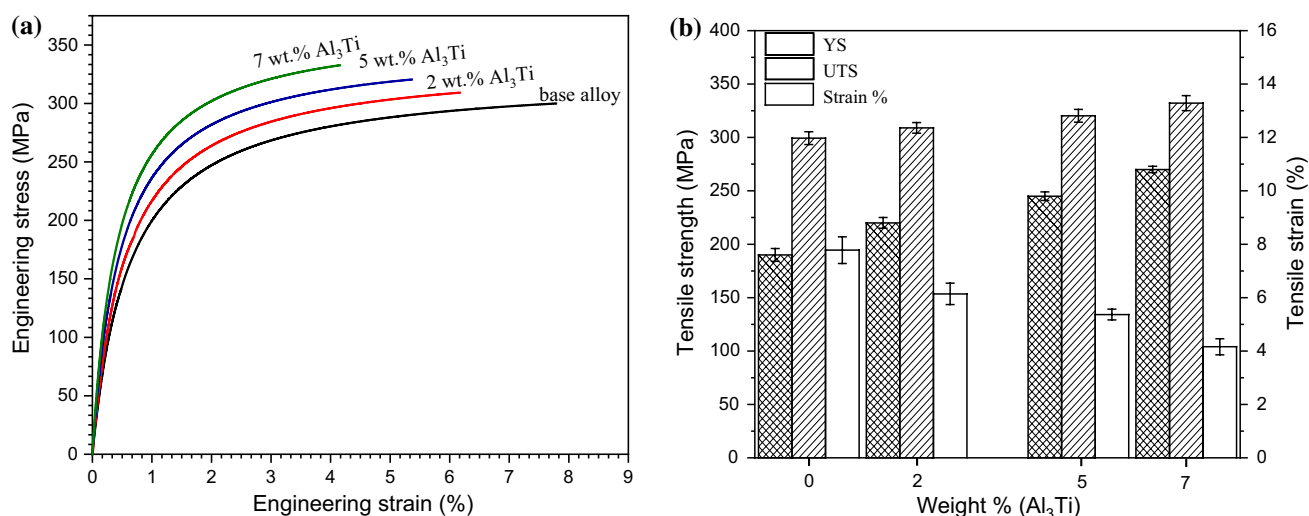
**Fig. 10** Tensile properties of the base alloy and in-situ composites. **a** tensile flow curves of the Al-7075 alloy and composites; and **b** variation of tensile properties with increasing Al$_3$Ti content
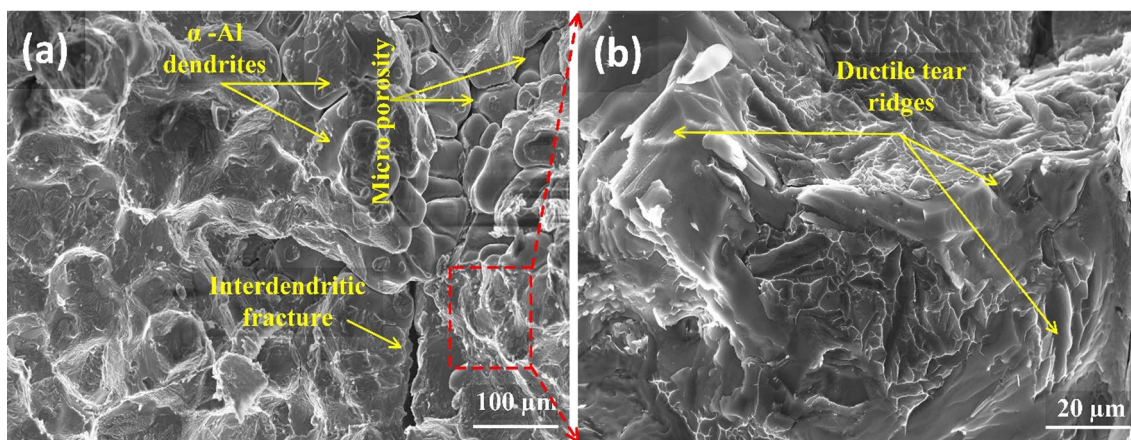


**Fig. 11** **a** FE-SEM image of the Al-7075 base alloy fractured surface; **b** corresponding magnified image

of the Ti particles inside the Al melt to form the Al$_3$Ti phase (Fig. 13b). Moreover, these shock waves were responsible for the even particle distribution and degassing. The micro-hotspots generated by cavitation stayed only for a few nanoseconds inside the molten melt during the UST. The temperature in such hotspots reaches up to 5000 °C with a cooling rate of approximately $10^{10}$ Ks$^{-1}$, and the localized pressure reaches approximately 1000 atm [33]; (iii) complete diffusion. The Al melt was held at 800 °C for 45 min to ensure the complete formation of Al$_3$Ti by diffusion of a large number of Al atoms in Ti for a thermodynamically stable interface configuration between the Al matrix and Al$_3$Ti particles (Fig. 13c); and (iv) the final degassing and particle distribution was carried out using UST (Fig. 13d) to ensure the formation of defect-free in-situ composites after the solidification process, as shown in Fig. 13e.

Uniform Al$_3$Ti particle distribution was achieved through the cavitation phenomenon. The traveling wave acoustic pressure was calculated as follows:

$$P_k = \sqrt{\frac{2P_t \cdot v \cdot \rho_L}{S_t}}, \tag{1}$$

where $P_t$ (kW) is the power output of the ultrasonic transducer, $v$ (ms$^{-1}$) is the sound velocity inside the melt, $\rho_L$ (g/cm$^3$) is the Al-melt density, and $S_t$ (cm$^2$) is the face area of the transducer probe [34, 35]. In the present study, $\rho_L = 2.81$ g/cm$^3$, $v = 4.58 \times 10^3$ ms$^{-1}$ for the Al melt [36], $P_t = 2.0$ kW and $S_t = 9.62$ cm$^2$. Therefore, the value of $P_k$ was calculated to be 7.62 MPa, which is much greater than the threshold value for generating sono-acoustic cavitation (1 MPa) [37], as shown in Fig. 14.
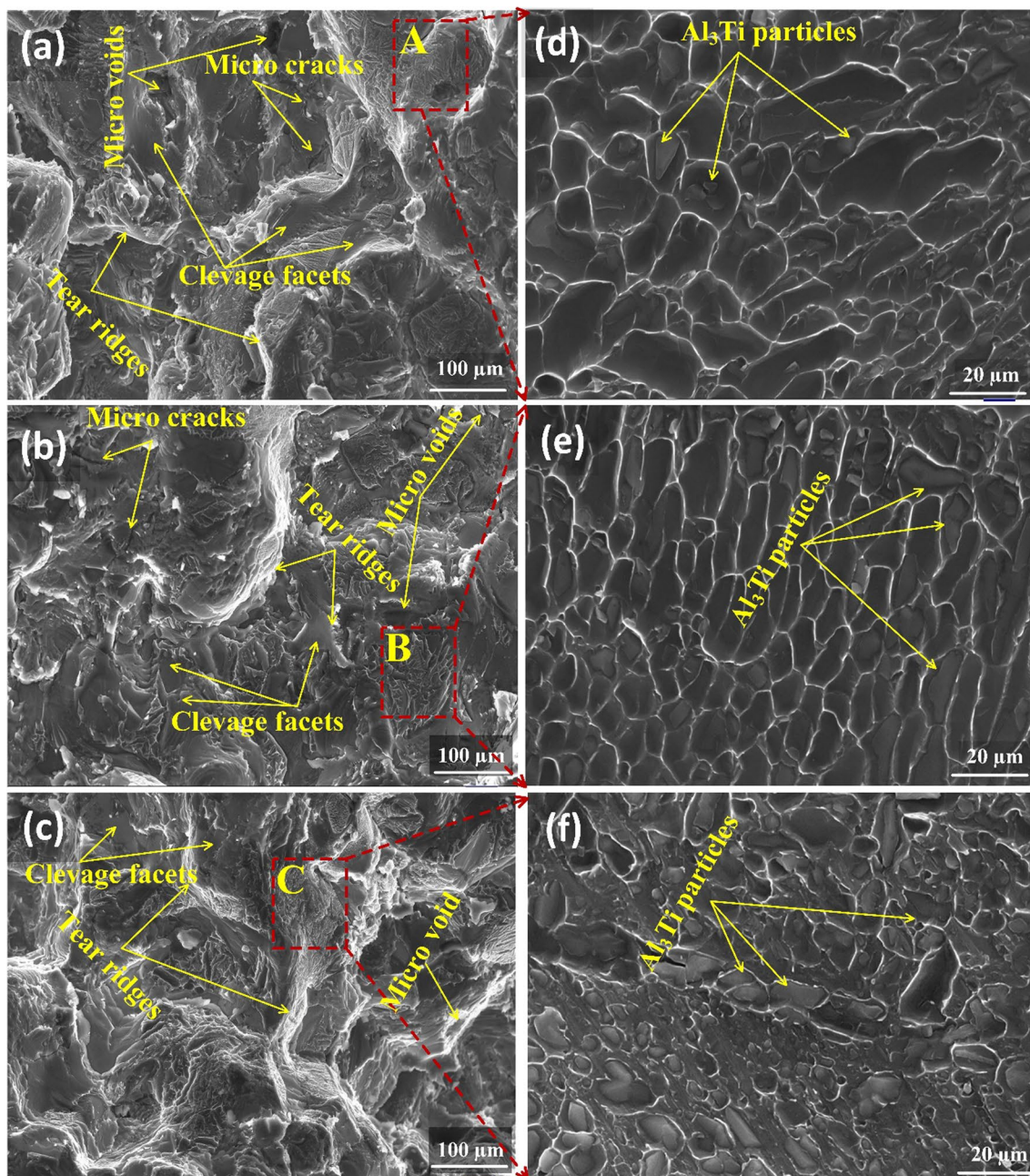
**Fig. 12** FE-SEM fracture images of the composites after the tensile test. **a** 2 wt% Al₃Ti; **b** 5 wt% Al₃Ti; **c** 7 wt% Al₃Ti; and **d–f** show the corresponding magnified portions (A, B, C)

The Ti particle clusters were fragmented at the micron level and dispersed evenly throughout the matrix owing to the action of the high-pressure pulse. This dispersion was facilitated by the turbulence generated near the Ti particles by the cavitation bubbles. To induce an instantaneous exothermic reaction between the Ti particles and Al melt to produce clean in-situ micrometer-level reinforcements inside the matrix, fully developed cavitation should be induced inside the melt. The ultrasonic vibration intensity is defined as

$$I = \frac{1}{2}\rho_L \cdot v \cdot (2\pi f A)^2, \tag{2}$$

where $f$ is the frequency (Hz), and $A$ (μm) is the amplitude of the ultrasonic wave. In molten Al alloys, for fully developed cavitation, $I \geq 80$ W cm$^{-2}$ [38]. In the present
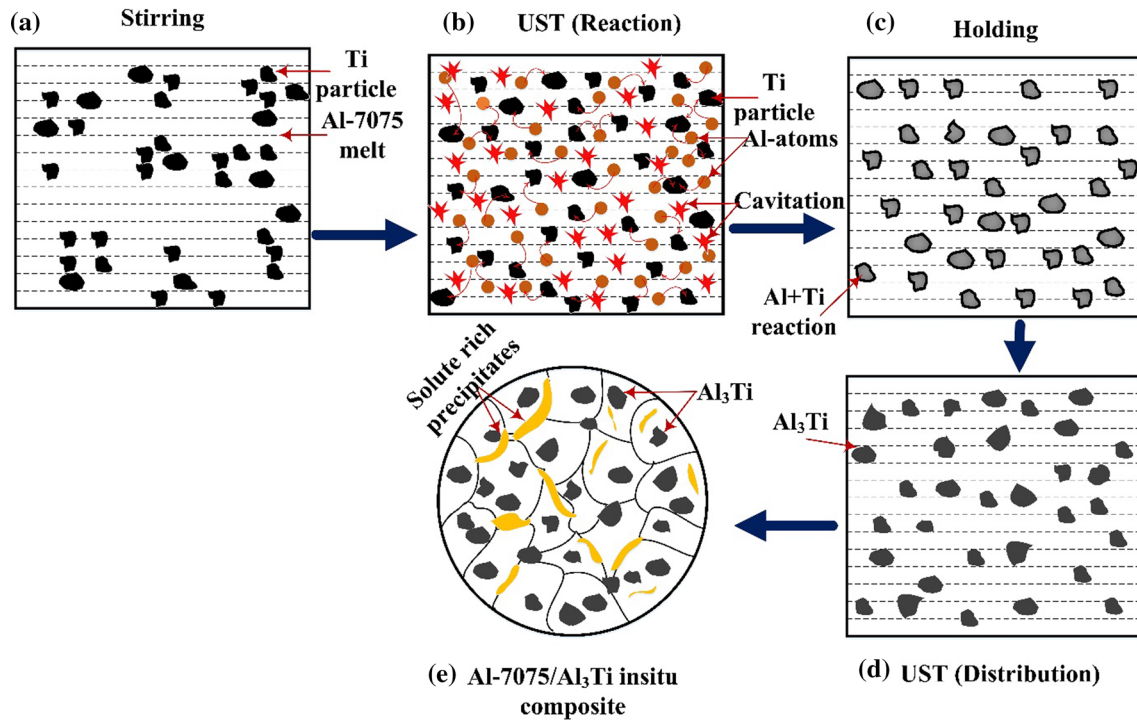
Fig. 13 Schematic illustration of the formation of Al$_3$Ti via SUST. a Ti powder mixing using impeller; b ultrasonic cavitation; c complete reaction of Ti with Al to form Al$_3$Ti; d fully developed Al$_3$Ti particle distribution under UST; and e as-cast Al-7075/Al$_3$Ti composites



Fig. 14 Schematic diagram of sono-acoustic cavitation
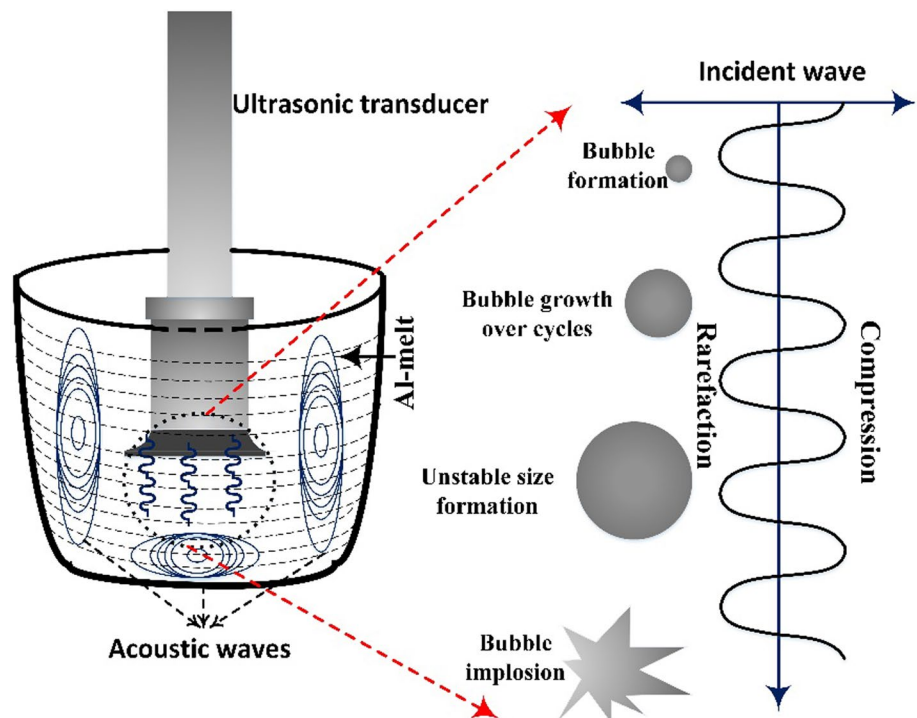
study, $A = 22$ μm, $f = 20 \times 10^3$ Hz, $\rho_L = 2.81$ g/cm$^3$, and $v = 4.58 \times 10^3$ m/s, resulting in $I = 1391$ W/cm$^2$. This is much greater than the threshold value for Al alloys (80 W/cm$^2$).

It is noteworthy that the cavitation effect indeed facilitated the even distribution of the Al$_3$Ti particles inside the matrix alloy, as shown in Fig. 6.

## 4.2 Interfacial Bonding Analysis

Interfacial energy significantly affects the wettability of the reinforcing phase and thus controls the mechanical properties of the composites to a great extent. In general, the interfacial energy is low when the interface between the secondary phase and substrate is coherent or partially coherent. According to Turnbull and Vonnegut, this coherency can be evaluated by the lattice misfit ($\delta$) between the matrix and the particle [39]. This misfit can be calculated using Eq. 3, where $a$ is the lattice constant. It is generally accepted that, when $\delta \leq 0.05$, the interface is coherent, and when $0.05 < \delta \leq 0.25$, the interface is partially coherent [40, 41].

$$\delta = \left[ \frac{a_{matrix} - a_{particle}}{a_{matrix}} \right] \tag{3}$$

The Al$_3$Ti crystal lattice consists of six Al and two Ti atoms in each unit cell and has a tetragonal geometry with the lattice parameters $a = b = 0.385$ nm and $c = 0.861$ nm. On the other hand, aluminum has a face-centered cubic geometry with $a = b = c = 0.404$ nm. The lattice misfits in both the $a$ and $b$ directions were calculated using the following equations: $\delta_{aa,bb} = (1 - a_{Al_3Ti}/a_{Al})$ and $\delta_{cc} = (1 - c_{Al_3Ti}/2a_{Al})$. The lattice mismatch for the $a$ and $b$ directions was found to be 0.047, while that for the $c$ direction was 0.065. This indicates that the in-situ Al$_3$Ti particles showed excellent lattice match with $\alpha$-Al in the $a$, $b$, and $c$ directions and formed a coherent boundary between $\alpha$-Al and Al$_3$Ti. The formation of coherent interface could be one of the reasons why the composites exhibited improved mechanical properties as compared to the base alloy.

## 4.3 Thermodynamics and Kinetics of Phase Transition During the UST

The grain refinement of the composites by the Al$_3$Ti particles (see Fig. 5) can be explained with the help of the aluminum-rich corner in the Al-Ti phase diagram. This phase diagram was generated using FactSage software and is shown in Fig. 15. At 665 °C, the peritectic reaction ($L + Al_3Ti \rightarrow \alpha Al$)) occurred. Considering the in-situ formation of the Al$_3$Ti particles, the degree of reaction between the solid Ti powders and molten Al alloy could be evaluated according to the following reaction.

$$3Al(L) + Ti(S) \rightarrow Al_3Ti(S) + \Delta H(\textit{Exothermic heat evolution}) \tag{4}$$
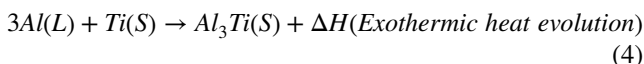
The exothermic heat of formation of the Al$_3$Ti particles is -35.6 kJ/g-atom, which caused localized melting at the interface, thus enhancing the reaction rate [42]. The
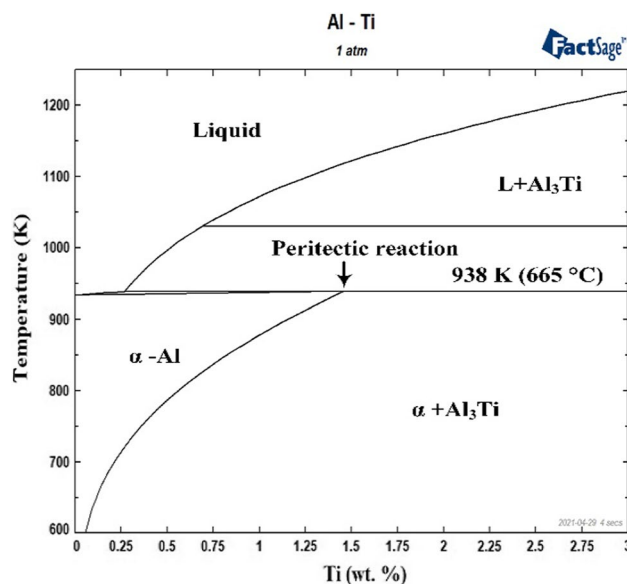


**Fig. 15** Al-rich corner of the Al-Ti phase diagram showing the peritectic reaction point at 665 °C

reaction product is $\alpha$-Al, which grows around the Al$_3$Ti particles, as indicated by the microstructures shown in Fig. 6. It is evident that the newly formed Al$_3$Ti particles acted as heterogeneous nucleation catalysts.

Cavitation-induced nucleation and even distribution are two major advantages often reported for UST [35]. When the UST is applied to the nucleation kinetics of the primary $\alpha$-Al phase, cooling-induced cavitation occurs because of the collapse of tiny bubbles and the formation of micro-hotspots. The large undercooling continues and creates micro-hotspots in various zones inside the melt, thus stimulating the creation of homogeneous nucleation sites in the alloy melt. This local undercooling can be explained by the Clausius Clapeyron theorem in Eq. 6. According to this theorem, an increase in the local pressure increases the freezing range of the alloy and promotes local undercooling [23].

$$\frac{\Delta T_f}{\Delta P} = \frac{T_f(V_l - V_s)}{\Delta H_f}, \tag{5}$$

where $T_f$ is the alloy freezing point, $P$ is the applied pressure, $V_l$ is the volume of the liquid phase, $V_S$ is the volume of the solid phase, and $\Delta H_f$ is the latent heat of fusion.

It has been reported that Al$_3$Ti particles can act as a substrate for heterogeneous nucleation, dramatically refining the $\alpha$-Al grains [19, 43, 44]. The presence of impurities on the surface of Al$_3$Ti influences its interfacial microstructure, adhesion strength, and bonding with the alloy matrix. The clean surface of Al$_3$Ti improves its wettability, thus reducing its contact angle, as shown in Fig. 16.
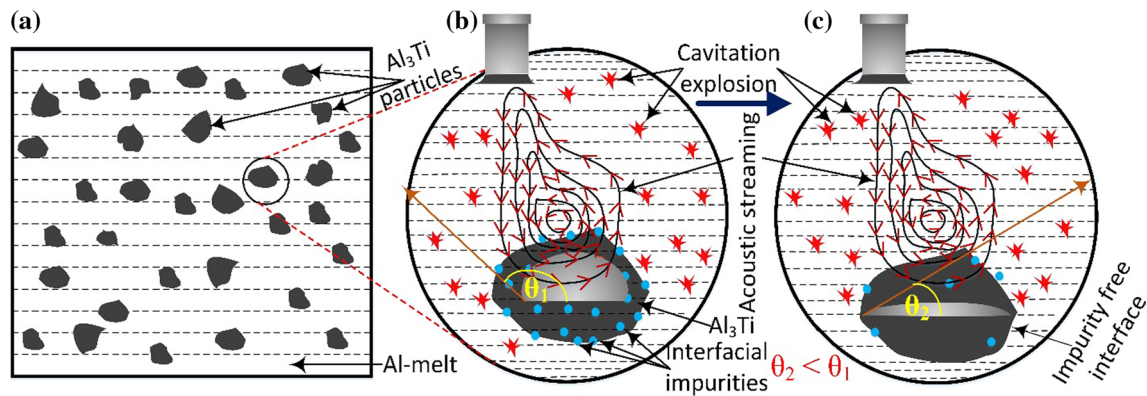
**Fig. 16** Improvement in the wettability of Al$_3$Ti under cavitation inside the Al melt during the solidification

The free energy barrier for heterogeneous nucleation on a substrate can be described by the classical nucleation theory [45].

$$\Delta G_{het} = \frac{16\pi(\gamma_{LC})^3 T_M^2}{3L^2 \Delta T_u^2}\left[\frac{(2+\cos\theta)(1-\cos\theta)2}{4}\right], \quad (6)$$

where $\gamma_{LC}$, $T_M$, $L$, $\Delta T_u$, and $\theta$ are the interfacial free energy between the liquid and solid interface, equilibrium melting temperature, latent heat of solidification, undercooling below the liquid temperature, and wetting angle between Al$_3$Ti and the liquid phase, respectively. As $\theta$ decreases, the energy barrier for heterogeneous precipitation at the Al/Al$_3$Ti interface also decreases. A reduction in the contact angle also increases the adhesion strength at the interface between Al$_3$Ti and the matrix alloy. Therefore, the UST delivers a clean surface to the Al$_3$Ti particles, thereby improving the heterogeneous nucleation of $\alpha$-Al crystals on the Al$_3$Ti substrate, as shown in Fig. 16c.

## 4.4 Strengthening Mechanisms

The strengthening mechanisms of the composites may include strengthening due to the grain refinement, load transfer effect, generation of dislocations by thermal expansion mismatch, and Orowan looping [46].

The increase in the YS of the composites was evaluated using both the continuum and micromechanical approaches. The continuum mechanics approach defines the direct load transfer effect due to the interfacial bonding of particles with the matrix. The micromechanics approach defines the load transfer mechanism due to the strengthening effect generated inside the matrix phase in the presence of particles. The continuum mechanics contribution to YS of the composites ($\sigma_{yc}$) was defined by the shear lag model [47] which is given as follows:

$$\sigma_{yc} = \sigma_{ym}\left[V_p\left(\frac{2+S}{2}\right) + (1-V_p)\right], \quad (7)$$

where $\sigma_{ym}$ represents the YS of the matrix phase and $V_p$ is the volume fraction of the reinforcing phase inside the matrix (0.016, 0.041, and 0.058 for the 2, 5, and 7 wt% Al$_3$Ti composites, respectively). The average aspect ratio of the particles, $S$, for all the composites was measured to be approximately 1.5.

The YS of the matrix ($\sigma_{ym}$) was evaluated by considering the grain refinement due to the UST and Ti addition ($\sigma_{HP}$), thermal expansion mismatch strengthening ($\Delta\sigma_{CTE}$), and Orowan strengthening ($\Delta\sigma_{Or}$) as follows [48]:

$$\sigma_{ym} = \sigma_o + \Delta\sigma_{HP} + \sqrt{\left(\Delta\sigma_{Or}\right)^2 + \left(\Delta\sigma_{CTE}\right)^2}, \quad (8)$$

where $\sigma_o$ is the YS of the cast matrix alloy (190 MPa in the present study).

The increase in the YS of the composites due to grain refinement as compared to that of the base alloy can be described by the Hall–Petch equation.

$$\Delta\sigma_{Hall-petch} = k\left(\frac{1}{\sqrt{d}} - \frac{1}{\sqrt{d_0}}\right) \quad (9)$$

where $k = 74$ MPa μm$^{1/2}$ for the Hall–Petch slope of aluminum alloys [49], and $d$ is the average grain size of the composites (65, 50, and 40 μm for the composites with 2, 5, and 7 wt% Al$_3$Ti, respectively). $d_o$ is the average grain size of the base alloy (160 μm).

The increase in the strength of the composites due to the thermal expansion coefficient (CTE) mismatch, $\Delta\alpha$, of the Al-7075 matrix ($25.9 \times 10^{-6}$ K$^{-1}$ [50]) and reinforcement ($3 \times 10^{-6}$ K$^{-1}$ [51]) can be expressed by Eq. 10. The difference in the CTE increases the dislocation density of the matrix surrounding the particles (known as the prismatic punching of dislocations) [52]. The accumulated

**Table 2** Contribution of various strengthening mechanisms to the YS of the composites

| UST-cast composites (wt%) | $\Delta\sigma_{Hall-petch}$ (MPa) | $\Delta\sigma_{CTE}$ (MPa) | $\sigma_{ym}$ (MPa) | $\sigma_{yc-Pred}$ (MPa) | $\sigma_{yc-expt}$ (MPa) | Absolute Error (%) |
|---|---|---|---|---|---|---|
| 2.0 | 3.6 | 12.5 | 206.1 | 212.6 | 200 | 6.1 |
| 5.0 | 4.9 | 22.4 | 217.3 | 228.1 | 208 | 9.6 |
| 7.0 | 6.2 | 29.9 | 226.1 | 245.1 | 218 | 12.3 |

dislocations at the matrix-particle interface significantly improves the YS of the composites.

$$\Delta\sigma_{CTE} = \beta Gb\sqrt{\rho},$$
$$\rho = \frac{12\Delta\alpha\Delta TV_p}{bd_p(1-V_p)}, \quad (10)$$

where $\beta$ is a constant (approximately equal to 1.25[53]); $G$ is the shear modulus of the Al matrix (26 GPa [54]); $b$ is the Burgers vector (0.286 nm [54]); $\Delta T$ is the difference between the stress-free homologue temperature, that is, the temperature at which the solidification started (943 K), and the mold temperature (308 K) after the solidification; and $d_p$ is the mean diameter of the Al$_3$Ti particles (10, 20, and 30 μm for the composites with 2, 5, and 7 wt% Al$_3$Ti, respectively).

The effect of Orowan strengthening can be quantified using the Orowan-Ashby equation:

$$\Delta\sigma_{Or} = \frac{0.13Gb}{\lambda}ln\frac{d_p}{2b}, \quad (11)$$

where $\lambda$ is the interparticle spacing in the matrix. With the application of a load, the dislocations interact with the particles. They first bow around and reconnect, leading to a good number of dislocation loops around the particles. The obstruction of the subsequent dislocation motion by the already generated dislocation loops improves the strength of the composites to a great extent. This mechanism becomes effective when the particle diameter is close to or less than 1 μm. Because the minimum average diameter of the particles was approximately 5 μm in this study, the contribution of Orowan strengthening was small. Hence, Eq. 12 can be reduced to

$$\sigma_{ym} = \sigma_o + \Delta\sigma_{HP} + \Delta\sigma_{CTE}. \quad (12)$$

The substitution of the different strengthening mechanisms into Eqs. 12 and 7 yields the value of $\sigma_{yc}$ for each composite, which was compared with the experimental results in Table 2. The predicted values of the YS for the composites with 2, 5, and 7 wt% Al$_3$Ti were 212.6, 228.1, and 245.1 MPa, respectively. The experimental corresponding values were 200, 208, and 218 MPa. This difference in the theoretical and measured values could be attributed to the presence of micropores, variations in the aspect ratio

and size of the particles, and size distribution of the grains in the matrix alloy. It must be noted that the thermal expansion mismatch was the dominant strengthening mechanism in the composites (Table 2).

## 5 Conclusions

An SUST approach was implemented for the fabrication of in-situ Al-7075/Al$_3$Ti MMCs. The following conclusions were drawn from the results and discussion.

1. Ti powders were added in stoichiometric proportions to the alloy melt for the direct reaction synthesis of Al$_3$Ti particles inside the as-cast matrix. The composites were fabricated under optimized casting variables, such as the stirring time, stirring velocity, holding time, sonication time, sonication frequency, and furnace temperature.
2. The high local temperature and pressure generated during ultrasonic cavitation accelerated the formation of the Al$_3$Ti reinforcing phase. In addition, the high local undercooling generated by the explosion of the cavitation bubbles led to the formation of many nucleation sites and refined the grains successfully as compared to the base alloy.
3. Microscopic analysis showed grain refinement and homogeneous distribution of the Al$_3$Ti particles in the matrix. Al$_3$Ti particles and the Al matrix generated clean and flawless interfaces, which improved the mechanical properties of the composites.
4. The YS, tensile strength, and hardness of the composites increased with an increase in the Al$_3$Ti content. Grain refinement, Thermal expansion mismatch, and interfacial adhesion between the matrix and reinforcement contributed to the high YS and tensile strength of the composites.

## Declarations

## References

1. D.B. Miracle, Metal matrix composites – From science to technological significance. Compos. Sci. Technol. **65**, 2526–2540 (2005). https://doi.org/10.1016/j.compscitech.2005.05.027

2. R. Aparicio-Fernández, H. Springer, A. Szczepaniak, H. Zhang, D. Raabe, In-situ metal matrix composite steels: Effect of alloying and annealing on morphology, structure and mechanical properties of TiB2 particle containing high modulus steels. Acta Mater. **107**, 38–48 (2016). https://doi.org/10.1016/j.actamat.2016.01.048

3. P. Samal, P.R. Vundavilli, A. Meher, M.M. Mahapatra, Recent progress in aluminum metal matrix composites: A review on processing, mechanical and wear properties. J. Manuf. Process. **59**, 131–152 (2020). https://doi.org/10.1016/j.jmapro.2020.09.010

4. S. Tang, C. Hu, Design, preparation and properties of carbon fiber reinforced ultra-high temperature ceramic composites for aerospace applications: a Review. J. Mater. Sci. Technol. **33**, 117–130 (2017). https://doi.org/10.1016/j.jmst.2016.08.004

5. J. Suthar, K.M. Patel, Processing issues, machining, and applications of aluminum metal matrix composites. Mater. Manuf. Process. **33**, 499–527 (2018). https://doi.org/10.1080/10426914.2017.1401713

6. P.K. Rohatgi, A. Kumar P., N.M. Chelliah, T.P.D. Rajan, Solidification Processing of Cast Metal Matrix Composites Over the Last 50 Years and Opportunities for the Future. JOM **72**, 2912–2926 (2020). https://doi.org/10.1007/s11837-020-04253-x

7. X. Rong, D. Zhao, C. He, C. Shi, E. Liu, N. Zhao, Revealing the strengthening and toughening mechanisms of Al-CuO composite fabricated via in-situ solid-state reaction. Acta Mater. **204**, 116524 (2021). https://doi.org/10.1016/j.actamat.2020.116524

8. K. Amouri, S. Kazemi, A. Momeni, M. Kazazi, Microstructure and mechanical properties of Al-nano/micro SiC composites produced by stir casting technique. Mater. Sci. Eng. A **674**, 569–578 (2016). https://doi.org/10.1016/j.msea.2016.08.027

9. M. Sarma, I. Grants, T. Herrmannsdörfer, G. Gerbeth, Contactless generation of cavitation in high temperature liquid metals and its impact on particle dispersion in solidified iron and steel samples. J. Mater. Process. Tech. **291**, 117041 (2021). https://doi.org/10.1016/j.jmatprotec.2021.117041

10. Q. Han, Ultrasonic processing of materials. Metall. Mater. Trans. B **46**, 1603–1614 (2015). https://doi.org/10.1007/s11663-014-0266-x

11. D.G. Eskin, Ultrasonic processing of molten and solidifying aluminium alloys: overview and outlook. Mater. Sci. Technol. (United Kingdom) **33**, 636–645 (2017). https://doi.org/10.1080/02670836.2016.1162415

12. Z. Liu, Z. Dong, X. Cheng, Q. Zheng, J. Zhao, Q. Han, On the supplementation of magnesium and usage of ultrasound stirring for fabricating in situ TiB2/A356 composites with improved mechanical properties. Metall. Mater. Trans. A **49**, 5585–5598 (2018). https://doi.org/10.1007/s11661-018-4883-x

13. R.V. Kumar, R. Keshavamurthy, C.S. Perugu, P.G. Koppad, M. Alipour, Influence of hot rolling on microstructure and mechanical behaviour of Al6061-ZrB2 in-situ metal matrix composites.

14. Mater. Sci. Eng. A **738**, 344–352 (2018). https://doi.org/10.1016/j.msea.2018.09.104

14. S. Komarov, Y. Ishiwata, I. Mikhailov, Industrial application of ultrasonic vibrations to improve the structure of Al-Si hypereutectic alloys: Potential and limitations. Metall. Mater. Trans. A **46**, 2876-2883 (2015). https://doi.org/10.1007/s11661-015-2829-0

15. T. Paul, C. Zhang, N. Denis, B. Boesl, A. Agarwal, Role of ultrasonic treatment on microstructure, mechanical and tribological behavior of 2D boron nitride reinforced aluminum composites. Mater. Sci. Eng. A **809**, 140970 (2021). https://doi.org/10.1016/j.msea.2021.140970

16. F. Wang, D. Eskin, J. Mi, C. Wang, B. Koe, A. King, C. Reinhard, T. Connolley, A synchrotron X-radiography study of the fragmentation and refinement of primary intermetallic particles in an Al-35 Cu alloy induced by ultrasonic melt processing. Acta Mater. **141**, 142–153 (2017). https://doi.org/10.1016/j.actamat.2017.09.010

17. V. Abbasi Chianeh, H.R. Madaah Hosseini, M. Nofar, Micro structural features and mechanical properties of Al-Al3Ti composite fabricated by in-situ powder metallurgy route. J. Alloy. Compd. **473**, 127–132 (2009). https://doi.org/10.1016/j.jallcom.2008.05.068

18. F. Wang, D. Eskin, J. Mi, T. Connolley, J. Lindsay, M. Mounib, A refining mechanism of primary Al3Ti intermetallic particles by ultrasonic treatment in the liquid state. Acta Mater. **116**, 354–363 (2016). https://doi.org/10.1016/j.actamat.2016.06.056

19. J. Li, M. Zhang, Y. Zhou, G. Chen, First-principles study of Al/Al 3 Ti heterogeneous nucleation interface. Appl. Surf. Sci. **307**, 593–600 (2014). https://doi.org/10.1016/j.apsusc.2014.04.079

20. G. Wang, M.S. Dargusch, M. Qian, D.G. Eskin, D.H. StJohn, The role of ultrasonic treatment in refining the as-cast grain structure during the solidification of an Al-2Cu alloy. J. Cryst. Growth. **408**, 119–124 (2014). https://doi.org/10.1016/j.jcrysgro.2014.09.018

21. H.M. Vishwanatha, J. Eravelly, C.S. Kumar, S. Ghosh, Dispersion of ceramic nano-particles in the Al-Cu alloy matrix using two-step ultrasonic casting and resultant strengthening. Mater. Sci. Eng. A **708**, 222–229 (2017). https://doi.org/10.1016/j.msea.2017.09.117

22. Z. Liu, Q. Han, J. Li, W. Huang, Effect of ultrasonic vibration on microstructural evolution of the reinforcements and degassing of in situ TiB2p/Al-12Si-4Cu composites. J. Mater. Process. Tech. **212**, 365–371 (2012). https://doi.org/10.1016/j.jmatprotec.2011.09.021

23. D. Yuan, X. Yang, S. Wu, S. Lü, K. Hu, Development of high strength and toughness nano-SiCp/A356 composites with ultrasonic vibration and squeeze casting. J. Mater. Process. Tech. **269**, 1–9 (2019). https://doi.org/10.1016/j.jmatprotec.2019.01.021

24. A.H. Idrisi, A.H.I. Mourad, Conventional stir casting versus ultrasonic assisted stir casting process: Mechanical and physical characteristics of AMCs. J. Alloy. Compd. **805**, 502–508 (2019). https://doi.org/10.1016/j.jallcom.2019.07.076

25. S.Y. Park, W.J. Kim, Difference in the Hot compressive behavior and processing maps between the as-cast and homogenized Al-Zn-Mg-Cu (7075) alloys. J. Mater. Sci. Technol. **32**, 660–670 (2016). https://doi.org/10.1016/j.jmst.2016.04.006

26. X. Li, J.J. Yu, Modeling the effects of Cu variations on the precipitated phases and properties of Al-Zn-Mg-Cu alloys. J. Mater. Eng. Perform. **22**, 2970–2981 (2013). https://doi.org/10.1007/s11665-013-0588-x

27. H. Sina, J. Corneliusson, K. Turba, S. Iyengar, A study on the formation of iron aluminide (FeAl) from elemental powders. J. Alloy. Compd. **636**, 261–269 (2015). https://doi.org/10.1016/j.jallcom.2015.02.132

28. R. Ghiaasiaan, B.S. Amirkhiz, S. Shankar, Quantitative metallography of precipitating and secondary phases after strengthening treatment of net shaped casting of Al-Zn-Mg-Cu (7000) alloys.

Mater. Sci. Eng. A **698**, 206–217 (2017). https://doi.org/10.1016/j.msea.2017.05.047

29. P.K. Krishnan, J.V. Christy, R. Arunachalam, A.H.I. Mourad, R. Muraliraja, M. Al-Maharbi, V. Murali, M.M. Chandra, Production of aluminum alloy-based metal matrix composites using scrap aluminum alloy and waste materials: Influence on microstructure and mechanical properties. J. Alloy. Compd. **784**, 1047–1061 (2019). https://doi.org/10.1016/j.jallcom.2019.01.115

30. S. Sharma, S.P. Dwivedi, Effects of waste eggshells and SiC addition on specific strength and thermal expansion of hybrid green metal matrix composite. J. Hazard. Mater. **333**, 1–9 (2017). https://doi.org/10.1016/j.jhazmat.2017.01.002

31. S. Lin, C. Aliravci, M.O. Pekguleryuz, Hot-tear susceptibility of aluminum wrought alloys and the effect of grain refining. Metall. Mater. Trans. A **38**, 1056–1068 (2007). https://doi.org/10.1007/s11661-007-9132-7

32. A. Pineau, A.A. Benzerga, T. Pardoen, Failure of metals I: Brittle and ductile fracture. Acta Mater. **107**, 424–483 (2016). https://doi.org/10.1016/j.actamat.2015.12.034

33. Y. Yang, J. Lan, X. Li, Study on bulk aluminum matrix nanocomposite fabricated by ultrasonic dispersion of nano-sized SiC particles in molten aluminum alloy. Mater. Sci. Eng. A **380**, 378–383 (2004). https://doi.org/10.1016/j.msea.2004.03.073

34. Z. Liu, M. Rakita, W. Xu, X. Wang, Q. Han, Ultrasound assisted salts-metal reaction for synthesizing TiB2 particles at low temperature. Chem. Eng. J. **263**, 317–324 (2015). https://doi.org/10.1016/j.cej.2014.11.043

35. G.I. Eskin, D.G. Eskin, Ultrasonic Treatment of Light Alloy Melts. CRC Press (2014). https://doi.org/10.1201/b17270

36. J.G. Jung, T.Y. Ahn, Y.H. Cho, S.H. Kim, J.M. Lee, Synergistic effect of ultrasonic melt treatment and fast cooling on the refinement of primary Si in a hypereutectic Al–Si alloy. Acta Mater. **144**, 31–40 (2018). https://doi.org/10.1016/j.actamat.2017.10.039

37. J. Li, T. Momono, Y. Tayu, Y. Fu, Application of ultrasonic treating to degassing of metal ingots. Mater. Lett. **62**, 4152–4154 (2008). https://doi.org/10.1016/j.matlet.2008.06.016

38. A. Ramirez, M. Qian, B. Davis, T. Wilks, D.H. StJohn, Potency of high-intensity ultrasonic treatment for grain refinement of magnesium alloys. Scr. Mater. **59**, 19–22 (2008). https://doi.org/10.1016/j.scriptamat.2008.02.017

39. D. Turnbull, B. Vonnegut, Nucleation Catalysis. Ind. Eng. Chem. **44**, 1292–1298 (1952). https://doi.org/10.1021/ie50510a031

40. H. Zhuo, J. Tang, N. Ye, A novel approach for strengthening Cu-Y2O3 composites by in situ reaction at liquidus temperature. Mater. Sci. Eng. A **584**, 1–6 (2013). https://doi.org/10.1016/j.msea.2013.07.007

41. L. Zhong, C. Deng, X. Zhang, H. Bai, J. Zhu, Z. Lu, Y. Xu, WC-Fe layer with high volume fraction and fracture toughness on cast iron fabricated by in situ solid-phase diffusion. Vacuum **168**, 108801 (2019). https://doi.org/10.1016/j.vacuum.2019.108801

42. H.C. Madhu, V. Edachery, K.P. Lijesh, C.S. Perugu, S.V. Kailas, Fabrication of wear-resistant Ti3AlC2/Al3Ti hybrid aluminum composites by friction stir processing. Metall. Mater. Trans. A **51**, 4086–4099 (2020). https://doi.org/10.1007/s11661-020-05821-1

43. R. Yang, Z. Zhang, Y. Zhao, G. Chen, Y. Guo, M. Liu, J. Zhang, Effect of multi-pass friction stir processing on microstructure and mechanical properties of Al3Ti/A356 composites. Mater. Charact. **106**, 62–69 (2015). https://doi.org/10.1016/j.matchar.2015.05.019

44. Y. Birol, A novel Al-Ti-B alloy for grain refining Al-Si foundry alloys. J. Alloy. Compd. **486**, 219–222 (2009). https://doi.org/10.1016/j.jallcom.2009.07.064

45. Y. Watanabe, Review on nucleation catalysis of tetragonal D022 Al3Ti and L12 modified (Al1−xMex)3Ti intermetallic compounds for solidification of alpha-Al grains. Catal. Today. (2020). https://doi.org/10.1016/j.cattod.2020.07.011

46. J. Li, F. Wang, C. Shi, E. Liu, C. He, N. Zhao, High strength-ductility synergy of MgAlB4 whisker reinforced aluminum matrix composites achieved by in situ synthesis. Mater. Sci. Eng. A **799**, 140127 (2021). https://doi.org/10.1016/j.msea.2020.140127

47. Y. Shan, B. Pu, E. Liu, C. Shi, C. He, N. Zhao, In-situ synthesis of CNTs@Al2O3 wrapped structure in aluminum matrix composites with balanced strength and toughness, Mater. Sci. Eng. A **797**, 140058 (2020). https://doi.org/10.1016/j.msea.2020.140058.

48. F. Chen, Z. Chen, F. Mao, T. Wang, Z. Cao, TiB2 reinforced aluminum based in situ composites fabricated by stir casting. Mater. Sci. Eng. A **625**, 357–368 (2015). https://doi.org/10.1016/j.msea.2014.12.033

49. N. Srivastava, G.P. Chaudhari, Microstructural evolution and mechanical behavior of ultrasonically synthesized Al6061-nano alumina composites. Mater. Sci. Eng. A **724**, 199–207 (2018). https://doi.org/10.1016/j.msea.2018.03.092

50. J.T. Wang, L. Xie, Z.G. Wang, H. Gu, K.Y. Luo, Y.L. Lu, M.T. He, M.Z. Ge, Influence of laser shock peening on the coefficient of thermal expansion of Al (7075)-based hybrid composites, J. Alloy. Compd. **844**, 156088 (2020). https://doi.org/10.1016/j.jallcom.2020.156088.

51. T. Li, E. Al Olevsky, M.A. Meyers, The development of residual stresses in Ti6Al4V-Al3Ti metal-intermetallic laminate (MIL) composites, Mater. Sci. Eng. A **473**, 49–57 (2008). https://doi.org/10.1016/j.msea.2007.03.069.

52. R. George, K.T. Kashyap, R. Rahul, S. Yamdagni, Strengthening in carbon nanotube/aluminium (CNT/Al) composites. Scr. Mater. **53**, 1159–1163 (2005). https://doi.org/10.1016/j.scriptamat.2005.07.022

53. M. Wang, D. Chen, Z. Chen, Y. Wu, F. Wang, N. Ma, H. Wang, Mechanical properties of in-situ TiB2/A356 composites. Mater. Sci. Eng. A **590**, 246–254 (2014). https://doi.org/10.1016/j.msea.2013.10.021

54. Q. Zhang, D.L. Chen, A model for predicting the particle size dependence of the low cycle fatigue life in discontinuously reinforced MMCs. Scr. Mater. **51**, 863–867 (2004). https://doi.org/10.1016/j.scriptamat.2004.07.006